

## Nanolaminated $\text{Fe}_2\text{AB}_2$ and $\text{Mn}_2\text{AB}_2$ ( $A = \text{Al, Si, Ga, In}$ ) materials and the assessment of their electronic correlations

Edirisuriya M. Dilanga Siriwardane<sup>1</sup>, Turan Birol,<sup>2</sup> Onur Erten,<sup>3</sup> and Deniz Çakır<sup>4,\*</sup>

<sup>1</sup>Department of Physics, University of Colombo, Colombo 00300, Sri Lanka

<sup>2</sup>Department of Chemical Engineering and Materials Science, University of Minnesota, Minneapolis, MN 55455, USA

<sup>3</sup>Department of Physics, Arizona State University, Tempe, AZ 85287, USA

<sup>4</sup>Department of Physics and Astrophysics, University of North Dakota, Grand Forks, North Dakota 58202, USA



(Received 16 June 2021; revised 1 November 2022; accepted 8 December 2022; published 28 December 2022)

Ternary transition metal carbides and nitrides in the so-called MAX phases constitute a rich family of compounds that host interesting electronic and magnetic properties, and thus, these materials have been drawing increasing levels of attention. Similar ternary boride compounds, the MAB phases, have been studied much less despite being equally if not more promising. In this paper, we investigate  $\text{Fe}_2\text{AB}_2$  and  $\text{Mn}_2\text{AB}_2$  ( $A = \text{Al, Si, Ga, and In}$ ) ternary layered transition metal borides with orthorhombic, hexagonal, and tetragonal crystal structures using first-principles density functional theory (DFT). We assess the reliability of different exchange-correlation functionals for the accurate prediction of the material properties of MAB phases. In addition to the electronic and crystal structures of  $\text{Fe}_2\text{AB}_2$  and  $\text{Mn}_2\text{AB}_2$  ( $A = \text{Ga, In, and Si}$ ), we predict the dynamical and thermodynamic stabilities against the competing phases. We conducted bonding analysis to comprehend the bonding characteristic between different atoms, which provides a fundamental understanding whether the exfoliation of these compounds into so-called two-dimensional MBene structures is likely or not. In addition to spin-polarized DFT+ $U$  calculations, which predict ordered magnetic moments, our DFT+embedded dynamical mean field theory calculations predict a significant degree of electronic correlations in the paramagnetic phase of these compounds. These calculations also predict the formation of fluctuating magnetic moments before the onset of a magnetic order in the MAB compounds like an earlier report on the MAX compound  $\text{Mn}_2\text{GaC}$ .

DOI: 10.1103/PhysRevMaterials.6.124005

### I. INTRODUCTION

Owing to their high melting points, hardness, electrical and thermal conductivities, inertness in many corrosive environments, and magnetic properties, transition metal borides have found uses in diverse applications, including wear-resistant coatings, cutting tools, thermal diffusion barriers, ohmic contacts, heterogeneous catalysis, high-temperature aerospace components, high-temperature electrodes, concentrated solar absorbers, permanent magnets, and primary battery electrodes [1].

Among the borides, MAB phases are layered ternary or quaternary compounds, where  $M$  stands for a transition metal element,  $A$  indicates a group III-A or IV-A element, and  $B$  is boron. MAB structures are composed of  $M$ -B sublattices interleaved by  $A$ -atom monolayers or bilayers. With the general formula  $(MB)_2A_m(MB_2)_n$  ( $n = 0, 1, 2, \dots$ ;  $m = 1, 2, 3, \dots$ ;  $M$  = transition metal;  $A$  = Al, Ga, In, Si, . . .), the rich chemistry of MABs offers impressive versatility and flexibility in designing materials with diverse properties. MAB materials emerge when one substitutes  $M$  (transition metal) and  $A$  elements (from group-III-A and IV-A) in the MAB phase. While the experimentally identified MAB phases with  $M_2\text{AlB}_2$  crystallize in the orthorhombic  $Cmmm$  structure,

$\text{Ti}_2\text{InB}_2$  was predicted to have a hexagonal crystal structure [1,2]. In contrast to MAX phases, which are layered, hexagonal, early transition metal carbides and nitrides, there is a much more limited number of MAB phases. However, MAB phases crystallize in different crystal structures depending on the composition. This diversity of crystal structures strongly suggests that the properties of MAB phases are tunable through the crystal structure and composition control. Tuning the chemical composition offers an additional degree of freedom in the quest for stable materials with physical and chemical properties, appealing for both fundamental research and technological applications. Also, the thickness of the boride layers, the number of metal layers in between the boride layers, and the orientation of the boron subunits imply the superiority of MAB phases over MAX ones, with the thickness of the carbide component as the only variable for tuning the material properties.

$\text{Fe}_2\text{AlB}_2$  is an already synthesized ferromagnetic (FM) MAB phase with a Curie temperature of 270–320 K [1,3].  $\text{Fe}_2\text{AlB}_2$  has been widely studied due to its magnetocaloric behavior, excellent strength, high Curie temperature, etc. [3].  $\text{Mn}_2\text{AlB}_2$  is another already synthesized MAB compound, which is FM at low temperatures, but it exhibits an anti-ferromagnetic (AFM) order at room temperature [4,5]. The transition temperature of the AFM phase of  $\text{Mn}_2\text{AlB}_2$  was reported as  $313 \pm 2$  K [4]. In this paper, we exploit the chemical diversity and the crystal structure engineering of MAB

\*deniz.cakir@und.edu

phases, aiming to predict MAB phases and their exfoliation possibilities into magnetic MBene monolayers. We vary the *A* elements of  $\text{Fe}_2\text{AB}_2$  and  $\text{Mn}_2\text{AB}_2$  compounds and study the stability. We select Al, Si, Ga, and In as the *A* element and reveal the magnetic properties, dynamical, mechanical, and phase stabilities of the aforementioned materials.

An additional interesting question about the MAB phases is their proximity to a magnetic quantum critical point. While many of these compounds are magnetically ordered, formation of local moments above the magnetic ordering temperature would suggest that even the compounds that do not magnetically order may be easily driven into a magnetic phase through doping. (This is the case in the MAX compound  $\text{Cr}_2\text{GeC}$ , which becomes a robust FM when Mn doped and hence is considered close to a FM quantum critical point [6].) To assess this possibility, we also performed density functional theory (DFT) + embedded dynamical mean field theory (eDMFT) calculations and calculated the  $\langle S_z^2 \rangle$  expectation value in the paramagnetic phase.

## II. COMPUTATIONAL METHODS

We carried out collinear spin-polarized first-principles calculations based on DFT as implemented in the Vienna *Ab initio* Simulation Package (VASP) [7–10]. The electron-ion interactions were considered by employing the projector augmented-wave method [11,12] with an energy cutoff value of 500 eV. The generalized gradient approximation (GGA) within Perdew-Burke-Ernzerhof (PBE) formalism [13,14] was employed. The strongly constrained and appropriately normalized (SCAN) [15] meta-GGA functional and GGA+*U* (*U* = 0–4 eV) [16] were also considered to assess the impact of different methods on the properties of MAB phases. Meta-GGA functionals also consider the kinetic energy density of the noninteracting electrons, which has been demonstrated to improve on the standard GGA functional in several systems with various types of bonding. [17–20].

The energy convergence criterion was set to  $10^{-6}$  eV/cell, while the force convergence criterion of the ionic steps was  $10^{-2}$  eV/Å. Tighter criteria were used for phonon and elastic constant calculations. Here,  $\Gamma$ -centered  $16 \times 4 \times 16$ ,  $16 \times 16 \times 8$ , and  $16 \times 16 \times 8$  Monkhorst-Pack *k* points were used for the structural relaxations of orthorhombic, hexagonal, and tetragonal phases, respectively. The supercell approach and the

force-constant method were employed to calculate the phonon dispersion using the PHONOPY code [21]. A  $4 \times 1 \times 4$  ( $4 \times 4 \times 2$ ) supercell for orthorhombic (hexagonal and tetragonal) structure(s) with *k*-points mesh of  $4 \times 4 \times 4$  was constructed to calculate the resulting forces on the perturbed atoms. The elastic constants were determined by using the density functional perturbation theory (DFPT) as implemented in the VASP code [22].

We also performed charge self-consistent DFT+eDMFT calculations using the Rutgers DFT+eDMFT implementation and the continuous time quantum Monte Carlo impurity solver [23–25]. All DMFT calculations are performed at fixed temperature of  $\beta = 1/k_B T = 50$  eV<sup>-1</sup>, which corresponds to  $T = 232$  K. The hybridization window is chosen to be  $\mp 10$  eV near the Fermi level, and  $U = 10$  eV and  $J = 0.7$  eV, which have been previously shown to work well in early 3d transition metals for this implementation [26]. This value is much larger than that used in DFT+*U* and possibly other DFT+DMFT implementations due to the fact that the dynamical screening processes are explicitly considered in DFT+DMFT, and compared with the other DMFT implementations where the +*U* correction is often applied on a Wannier orbital, the implementation we use employs projections onto atomic orbitals of often smaller volume. A discussion of the predicted correlation strength and comparisons with angle-resolved photoemission spectroscopy (ARPES) studies on MAX phases is presented in Sec. IV. The bandwidth renormalization factor is calculated from the imaginary part of the self-energy on the imaginary axis [27], as explained in Ref. [28], using the first five Matsubara frequencies.

## III. RESULTS AND DISCUSSION

The PBE-GGA exchange-correlation potential, known to inaccurately predict the electronic and magnetic properties of many well-known transition metal compounds, has been widely used for studying the properties of the MAB materials. Since the Mn and Fe elements contain *d* electrons, we attempted to investigate how the onsite Coulomb potential can affect the structure of the  $\text{Fe}_2\text{AB}_2$  and  $\text{Mn}_2\text{AB}_2$  materials. Due to the lack of a systematic guideline to determine the *U* parameters, we conducted a search to determine the appropriate *U* values that properly reproduce the structural parameters of experimentally synthesized  $\text{Fe}_2\text{AlB}_2$  [29] and  $\text{Mn}_2\text{AlB}_2$  [30].

TABLE I. The lattice constants (*a*, *b*, and *c*) and magnetic moment per Fe or Mn atom ( $\mu$ ) calculated with the PBE-GGA, PBE-GGA+*U*, and SCAN methods. Here, *U* values are given in electronvolts. An AFM configuration is considered for  $\text{Mn}_2\text{AlB}_2$ , where the lattice parameter is doubled in the *c* direction. We present half of the *c* parameter.

Material	Parameter	Experiment	<i>U</i> = 0	<i>U</i> = 2	<i>U</i> = 3	<i>U</i> = 4	SCAN
$\text{Fe}_2\text{AlB}_2$	<i>a</i> (Å)	2.92	2.92	2.91	2.91	2.93	2.88
	<i>b</i> (Å)	10.99	11.03	11.00	10.99	11.02	10.91
	<i>c</i> (Å)	2.86	2.85	2.88	2.88	2.90	2.85
	$\mu$ ( $\mu_{\text{B}}$ )	1.05–1.32 [31,32]	1.38	1.65	1.71	1.95	1.59
$\text{Mn}_2\text{AlB}_2$	<i>a</i> (Å)	2.92	2.89	3.00	3.01	3.05	2.95
	<i>b</i> (Å)	11.04	11.13	11.10	11.14	11.18	11.06
	<i>c</i> (Å)	2.89	2.83	3.07	3.22	3.53	2.90
	$\mu$ ( $\mu_{\text{B}}$ )	0.71 [4]	0.74	3.09	3.57	3.92	2.54

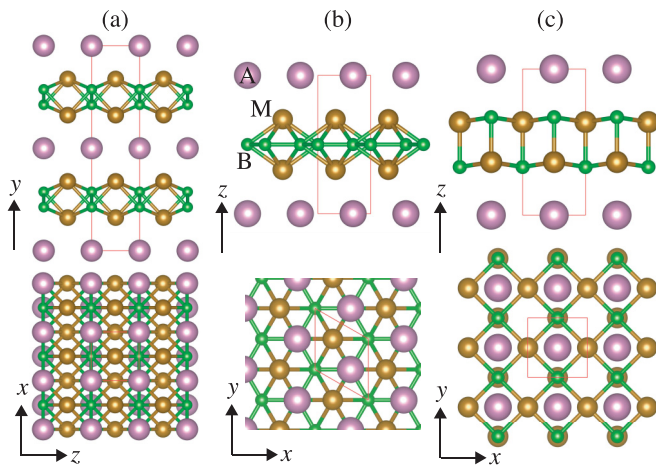


FIG. 1. Side and top views of the  $M_2\text{AB}_2$  materials with (a) orthorhombic, (b) hexagonal, and (c) tetragonal crystal symmetries. In the top row, the longest lattice parameter and corresponding axis are shown. Bottom row denotes the projection of the atoms on a plane perpendicular to the longest axis. Green, purple, and dark yellow spheres represent the B, A, and M atoms, respectively.

We computed the lattice parameters, cell volumes, and magnetic moments on transition metals of these two materials using GGA+ $U$  with different  $U$  values ( $U = 0\text{--}4$  eV), as well as SCAN, as summarized in Table I. Our GGA+ $U$  method was introduced by Dudarev *et al.* [16] and is an effective  $U$  approach where only  $U$  is defined as  $U_{\text{Eff}} = U - J$ . In this expression,  $J$  is set to zero; then  $U_{\text{Eff}} = U$ . Especially the lattice parameters of  $\text{Mn}_2\text{AlB}_2$  are significantly overestimated when we use GGA+ $U$  with a large  $U$  value. PBE-GGA ( $U = 0$ ) predicts structural parameters that are much closer to the experimental values for  $\text{Fe}_2\text{AlB}_2$  and  $\text{Mn}_2\text{AlB}_2$ . While GGA is appropriate to compute structural parameters, the prediction of magnetic properties may require the proper treatment of  $d$  orbitals which are the main source of magnetism in the examined structures. However, the PBE-GGA functional is also found to be better choice among the considered functionals for the prediction of magnetic moments on Fe and Mn atoms.

### A. Crystal symmetries and structures

We considered three different crystal symmetries, namely, orthorhombic ( $Cmmm$ ), hexagonal ( $P-6m2$ ), and tetragonal ( $P-4m2$ ), for  $\text{Fe}_2\text{AB}_2$  and  $\text{Mn}_2\text{AB}_2$  materials. The experimentally realized  $\text{Cr}_2\text{AlB}_2$ ,  $\text{Mn}_2\text{AlB}_2$ , and  $\text{Fe}_2\text{AlB}_2$  MAB phases crystallize in the orthorhombic ( $Cmmm$ ) structure [33,34]. Moreover,  $\text{Ti}_2\text{InB}_2$  was discovered to have hexagonal symmetry [2]. In this paper, we also considered a tetragonal crystal symmetry. This structure is included with the aim to realize a two-dimensional (2D) MBene with tetragonal symmetry from the parent tetragonal MAB phase. A tetragonal MBene monolayer with promising magnetic properties has been computationally reported [35]. Representative unit cells of orthorhombic, hexagonal, and tetragonal crystal structures are shown in Fig. 1.

A closer look indicates that the B atoms in the orthorhombic structure form one-dimensional zigzag chains extending

along the  $x$  direction, which are connected by transition metal atoms along the  $z$  direction. On the contrary, the B atoms form a honeycomb structure (on the  $xy$  plane) sandwiched between two atomic layers formed by the transition metal atoms in the hexagonal structure. For the tetragonal structure, the B atoms reside on the two different planes in the  $z$  direction. These two planes are connected by  $M\text{-B}$  bonds. The B-B bond lengths of orthorhombic and hexagonal structures are as small as 1.7 Å due to direct B-B bonding, whereas that of tetragonal counterparts are >2.5 Å. Depending on the magnetic order (i.e., FM vs AFM) and the A element, the smallest Fe-Fe and Mn-Mn distances in the hexagonal phase are  $\sim$ 2.50–2.60 Å and 2.55–2.70 Å, respectively. The predicted MAB phases have a layered morphology with an internal structure of alternate stacking of A element planes and  $M_2\text{B}_2$  sheets along the  $y$  axis for the orthorhombic phase and the  $z$  axis for the hexagonal and tetragonal phases. Therefore, in principle, one can synthesize 2D MBenes using any of these structures with different crystal symmetries by etching out the A layers like the synthesis of MXenes from MAX phases. However, we should note that the etching process of MAB phases is very challenging and may require very different experimental conditions.

### B. Energetic and magnetic properties

After determining the crystal structures and symmetries, we studied different spin configurations to find out the lowest energy magnetic states of  $\text{Fe}_2\text{AB}_2$  and  $\text{Mn}_2\text{AB}_2$  materials. We considered five collinear AFM orderings for the orthorhombic and hexagonal structures, while four different AFM spin configurations were used for the tetragonal structure, as shown in Figs. 2–4. We labeled the AFM configurations as AFM-iO, AFM-iH, and AFM-iT, where  $i$  represents the index and O, H, and T denote the orthorhombic, hexagonal, and tetragonal crystal symmetries, respectively. We considered both interlayer (between  $M\text{-B}$  layers) and intralayer (within an  $M\text{-B}$  layer) AFM coupling. For instance, in AFM-3O, the neighboring  $M\text{-B}$  layers are coupled AFM. However, AFM-5O includes both interlayer and intralayer AFM couplings. As a first step, we determined the magnetic ground state (GS) using PBE-GGA, PBE-GGA +  $U$ , and SCAN. We summarize the magnetic GSs of the considered materials as a function of the functional in Table II and the Appendix. Before discussing the considered materials, we took experimentally sensitized FM orthorhombic  $\text{Fe}_2\text{AlB}_2$  and  $\text{Mn}_2\text{AlB}_2$  as representative systems to assess the functional dependence of magnetic moment on the transition metal atoms. For  $\text{Fe}_2\text{AlB}_2$ , the reported low-temperature magnetization values vary between 1.00 and  $1.32 \mu_B/\text{Fe}$  depending on the synthesis method [31,32].

Table II summarizes the GGA-PBE-calculated relative energies of all structures and magnetic states with respect to the lowest-energy structures. For instance, for  $\text{Fe}_2\text{GaB}_2$ -O (i.e., orthorhombic  $\text{Fe}_2\text{GaB}_2$ ), the lowest-energy magnetic state is FM, and it is 0.117 eV/f.u. more stable than the nonmagnetic (NM) state. It can be noted that the NM states of all the considered materials have higher total energies than both FM and AFM states. Thus,  $\text{Fe}_2\text{AB}_2$  and  $\text{Mn}_2\text{AB}_2$  compounds are either FM or AFM materials depending on the crystal structure and the type of A element. As an example,  $\text{Fe}_2\text{GaB}_2$  exhibits FM as the lowest-energy magnetic state for orthorhombic

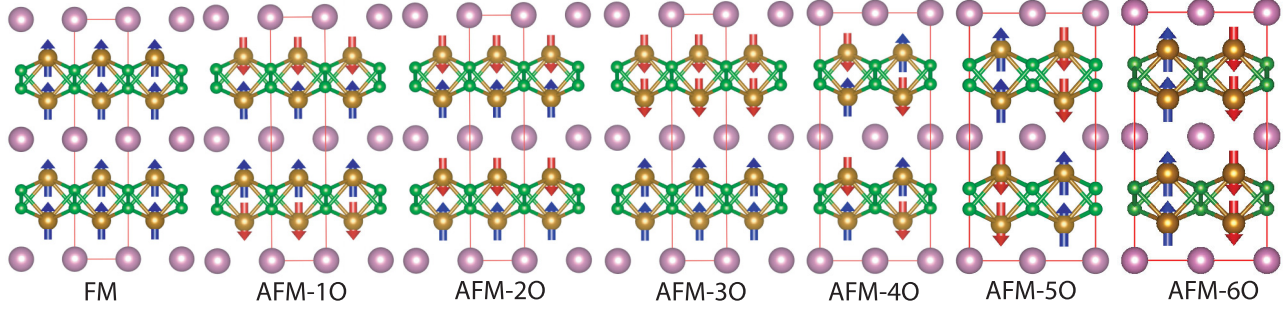


FIG. 2. Ferromagnetic (FM) and antiferromagnetic (AFM) spin configurations for the orthorhombic crystal structure. Green, purple, and dark yellow spheres represent the B, A, and M atoms, respectively.

structure, while hexagonal and tetragonal  $\text{Fe}_2\text{GaB}_2$  have AFM state as the lowest-energy magnetic configuration. Considering all crystal symmetries and magnetic structures for Fe-Ga based MAB phases, AFM-1H is the GS structure (i.e.,  $\Delta E = 0$  in Table II).  $\text{Fe}_2\text{InB}_2$  possesses the AFM-1H spin configuration as the GS structure, whereas the FM state is the GS structure for  $\text{Fe}_2\text{SiB}_2$  with orthorhombic symmetry (FM-O). AFM-1H is the lowest-energy structure for  $\text{Fe}_2\text{GaB}_2$  and  $\text{Fe}_2\text{InB}_2$ , and FM-O is for  $\text{Fe}_2\text{SiB}_2$ , regardless of the used functionals.

While Ga and In favor the hexagonal structure for Fe-based MAB systems, considering Si as an A element can facilitate the formation of the orthorhombic structure. Therefore, we can realize either orthorhombic or hexagonal crystal structures by selecting the appropriate A element. Similarly, hexagonal  $\text{Mn}_2\text{GaB}_2$  is FM (FM-H), while  $\text{Mn}_2\text{InB}_2$  and  $\text{Mn}_2\text{SiB}_2$  have AFM-3H and AFM-6O as GSs, respectively. In each transition metal-A element combination, the tetragonal phase is energetically unfavorable with a large positive energy difference ( $\Delta E$ ) with respect to the hexagonal and orthorhombic phases. Comparably, using Si as an A element may ease the synthesization of the tetragonal phase due to the small energy difference with orthorhombic or hexagonal structures (Table II). However, there are other tetragonal bulk structures of MAB phases with different crystal structures which have computationally been found to be stable, and some of them have been synthesized such as  $M_5\text{AB}_2$  compounds where M is typically Mn, Fe, or Co, and A can be Si, Ge, or P [36–38].

Our GGA-PBE calculations predict a value of  $1.37 \mu_B/\text{Fe}$  with fair agreement with experiment. Adding  $U$  or using SCAN increases the magnetic moment from the  $U = 0$  value

by  $0.2\text{--}0.3 \mu_B/\text{Fe}$ . In a previous work, the SCAN functional was shown to severely overestimate the magnetic moments in an itinerant electron FM [39]. We found a similar result for  $\text{Fe}_2\text{AlB}_2$  which is an itinerant electron FM.  $\text{Mn}_2\text{AlB}_2$  becomes a canted AFM (or AFM-6O shown in Fig. 2)  $<390 \text{ K}$  with a magnetic moment of  $0.71 \mu_B$  per Mn atom [4]. According to our calculations with GGA, the AFM configuration is by 42 meV/f.u. more stable than the FM phase. For the experimentally predicted AFM configuration, the magnetic moment is found to be  $0.74 \mu_B/\text{Mn}$ , which agrees well with the experimental measurements. When the  $U$  parameter varies as  $2 \rightarrow 3 \rightarrow 4 \text{ eV}$ , the magnetic moment on Mn atoms in the AFM configuration changes as  $3.09 \rightarrow 3.57 \rightarrow 3.92 \mu_B$ . SCAN makes a better prediction with a value of  $2.56 \mu_B$  than GGA +  $U$ . Fairly good agreement of lattice parameters, magnetic GSs, and magnetic moments with the experiment suggests that the PBE-GGA functional is appropriate to investigate Fe- and Mn-based MAB phases. In the rest of this paper, we only discuss results obtained within PBE-GGA ( $U = 0$ ).

### C. Dynamical stability

To examine the dynamical stability of the predicted MAB phases, we computed phonon dispersion curves for the GS structures. Since the PBE-GGA (with  $U = 0$ ) functional is sufficient to understand the structural and magnetic properties of the considered MAB phases, the phonon dispersions shown in Fig. 5 were obtained using PBE-GGA (with  $U = 0$ ) calculations. The absence of imaginary frequencies in the phonon dispersion spectra highlight the dynamical stability of the six considered systems in their respective GS magnetic

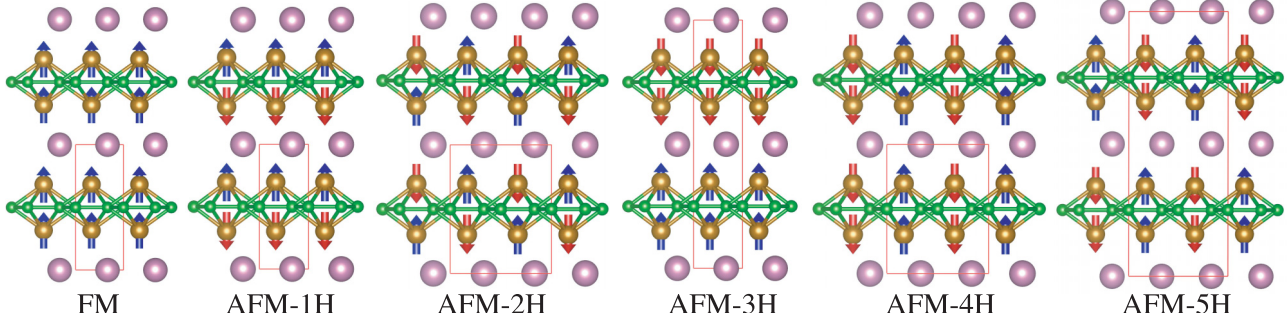


FIG. 3. Ferromagnetic (FM) and antiferromagnetic (AFM) spin configurations for the hexagonal crystal structure. Green, purple, and dark yellow spheres represent the B, A, and M atoms, respectively.

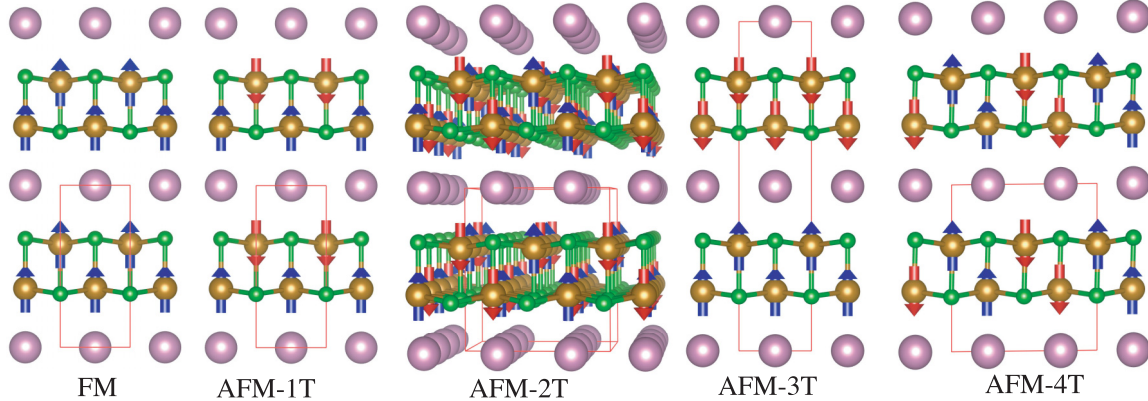


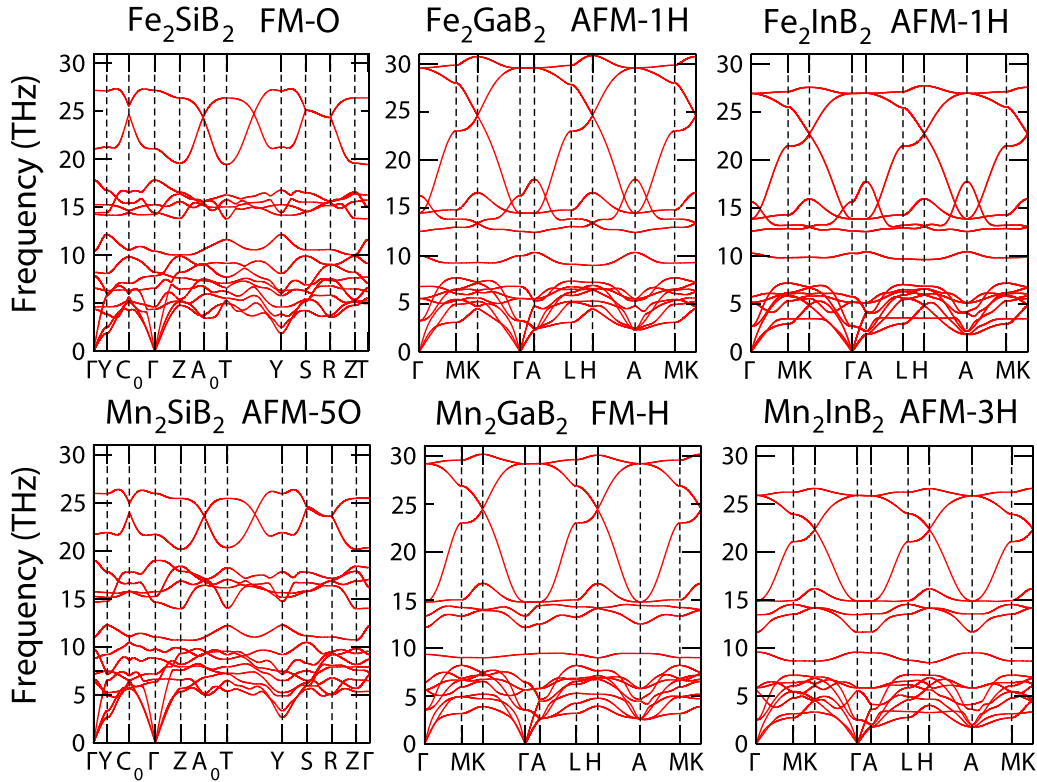
FIG. 4. Ferromagnetic (FM) and antiferromagnetic (AFM) spin configurations for the tetragonal crystal structure. Green, purple, and dark yellow spheres represent the B, A, and  $M$  atoms, respectively.

configuration. Since Ga and In are in the same column of the periodic table, MAB phases with those elements have very similar dispersion relations. Also, the maximum frequency of the optical phonons decreases as we move from Ga to In. This behavior is attributed to the fact that the vibrational frequencies are inversely proportional to the mass of atoms (In is  $\sim 2 \times$  heavier than Ga) and directly proportional to the stiffness of the bonds. For  $\text{Fe}_2\text{SiB}_2$  (FM-O) and  $\text{Mn}_2\text{SiB}_2$  (AFM-5O), even though the Fe atom is slightly heavier than the Mn atom, the frequencies of the two highest optical phonon branches are at slightly larger frequencies in the former. However,

in other branches, we have the reverse situation. These two systems have the same type of crystal structure but possess different magnetic GSs, which affects the force constants. Therefore, due to the small mass difference between Fe and Mn, a detailed force constant analysis should be done to make a reliable comparison. Similarly,  $\text{Fe}_2\text{InB}_2$  (AFM-1H) and  $\text{Mn}_2\text{InB}_2$  (AFM-3H) have similar frequency values for the same kind of phonon branch. Only the branches between 10 and 17 Thz exhibit substantially different variation over the Brillouin zone in these two systems where the vibrations of In and metal atoms are located.

TABLE II. GGA calculated relative energy (eV/f.u.) of NM, FM, and AFM phases with respect to the lowest energy magnetic states. In the last column,  $\Delta E$  represents the energy difference with respect to GS for each transition metal-A element (Si, Ga, In) combination.

Structure	NM	FM	AFM-1	AFM-2	AFM-3	AFM-4	AFM-5	AFM-6	$\Delta E$
$\text{Fe}_2\text{AlB}_2\text{-O}$	0.142	0.000	0.025	0.075	0.038	0.125	0.089	—	0.000
$\text{Fe}_2\text{AlB}_2\text{-H}$	0.115	0.108	0.000	0.093	0.079	0.115	0.114	—	0.400
$\text{Fe}_2\text{AlB}_2\text{-T}$	0.315	0.010	0.100	0.209	0.000	0.168	—	—	1.306
$\text{Fe}_2\text{SiB}_2\text{-O}$	0.106	0.000	0.022	0.111	0.080	0.106	0.106	0.101	0.000
$\text{Fe}_2\text{SiB}_2\text{-H}$	0.024	0.024	0.000	0.024	0.009	0.024	0.024	—	0.008
$\text{Fe}_2\text{SiB}_2\text{-T}$	0.226	0.007	0.014	0.129	0.000	0.109	—	—	0.787
$\text{Fe}_2\text{GaB}_2\text{-O}$	0.117	0.000	0.033	0.049	0.007	0.103	0.049	0.042	0.255
$\text{Fe}_2\text{GaB}_2\text{-H}$	0.155	0.143	0.000	0.123	0.102	0.147	0.147	—	0.000
$\text{Fe}_2\text{GaB}_2\text{-T}$	0.320	0.017	0.104	0.230	0.000	0.177	—	—	1.294
$\text{Fe}_2\text{InB}_2\text{-O}$	0.170	0.064	0.093	0.088	0.000	0.108	0.016	0.048	0.313
$\text{Fe}_2\text{InB}_2\text{-H}$	0.167	0.157	0.000	0.128	0.119	0.163	0.161	—	0.000
$\text{Fe}_2\text{InB}_2\text{-T}$	0.319	0.006	0.082	0.238	0.000	0.175	—	—	1.565
$\text{Mn}_2\text{AlB}_2\text{-O}$	0.056	0.038	0.056	0.053	0.056	0.056	0.024	0.000	0.000
$\text{Mn}_2\text{AlB}_2\text{-H}$	0.178	0.000	0.112	0.178	0.076	0.102	0.177	—	0.556
$\text{Mn}_2\text{AlB}_2\text{-T}$	0.057	0.032	0.055	0.056	0.000	0.052	—	—	1.563
$\text{Mn}_2\text{SiB}_2\text{-O}$	0.075	0.070	0.072	0.072	0.072	0.040	0.027	0.000	0.000
$\text{Mn}_2\text{SiB}_2\text{-H}$	0.103	0.001	0.002	0.086	0.000	0.068	0.104	—	0.140
$\text{Mn}_2\text{SiB}_2\text{-T}$	0.160	0.076	0.159	0.157	0.000	0.156	—	—	1.037
$\text{Mn}_2\text{GaB}_2\text{-O}$	0.079	0.062	0.079	0.079	0.078	0.079	0.029	0.000	0.085
$\text{Mn}_2\text{GaB}_2\text{-H}$	0.213	0.000	0.064	0.213	0.066	0.119	0.248	—	0.000
$\text{Mn}_2\text{GaB}_2\text{-T}$	0.097	0.027	0.095	0.097	0.000	0.088	—	—	1.331
$\text{Mn}_2\text{InB}_2\text{-O}$	0.000	0.000	0.000	0.000	0.000	0.000	0.000	0.000	0.304
$\text{Mn}_2\text{InB}_2\text{-H}$	0.383	0.031	0.031	0.327	0.000	0.266	0.305	—	0.000
$\text{Mn}_2\text{InB}_2\text{-T}$	0.272	0.000	0.252	0.272	0.012	0.196	—	—	1.420

FIG. 5. Phonon spectrum of the ground state structures of MAB phases, obtained with PBE-GGA (with  $U = 0$ ) calculations.

#### D. Mechanical properties

To shed some light on the mechanical stability, we calculated the elastic constants using DFPT. The elastic constants provide crucial information about the elastic deformation behavior of a solid. First of all, the elastic constants ( $C_{ij}$ ) of the materials should satisfy the Born-Huang criteria [40] if the material is mechanically stable. The mechanical stability criteria for the orthorhombic structures are  $C_{ii} > 0$ , ( $i = 1, 2, 3, 4, 5, 6$ ),  $C_{11}C_{22} - C_{12}^2 > 0$ ,  $C_{22}C_{33} - C_{23}^2 > 0$ ,  $C_{33}C_{11} - C_{31}^2 > 0$ , and  $C_{11}C_{22}C_{33} + 2C_{12}C_{23}C_{31} - C_{11}C_{23}^2 - C_{22}C_{31}^2 - C_{33}C_{12}^2 > 0$ . Similarly, the stability criteria for the hexagonal materials are as follows  $C_{44} > 0$ ,  $C_{11} - |C_{12}| > 0$ , and  $(C_{11} + C_{12})C_{33} - 2C_{13}^2 > 0$ . All the GS structures shown in Table III comply with the above requirements. Therefore, our predicted materials are mechanically stable. The elastic constants decrease when moving from Si  $\rightarrow$  Ga  $\rightarrow$  In. For the hexagonal phase, the calculated elastic

constant  $C_{11}$  (which is equal to  $C_{22}$ ) is larger than the other principal elastic constant  $C_{33}$ . Owing to the existence of strong boron-boron bonds, the hexagonal MAB crystals are harder to compress along the axes  $x$  and  $y$  than along the axis  $z$ . Similarly, the existence of the zigzag B-B chains along the  $x$  direction of the orthorhombic structures results in large elastic constants along this direction. We also calculated the elastic modulus ( $Y$ ), bulk modulus ( $K$ ), shear modulus ( $G$ ), and Poisson's ratio ( $\nu$ ) by employing the Voigt-Reuss-Hill approximation [42–44], as mentioned in Table IV. It is clear that Ga-based materials have higher  $Y$ ,  $K$ , and  $G$  values than that of In-based materials. In our previous paper, we showed that the  $M$ - $A$  and  $B$ - $A$  bond lengths (Bader charge transfer) increase (decreases) when  $A$  changes as Al  $\rightarrow$  Ga  $\rightarrow$  In in  $M_2AB_2$  compounds [45]. Thus, stronger Coulomb attraction within  $M$ -Al and B-Al bonds are available than that of Ga- and In-related bonds. The stronger bonds in  $M_2AlB_2$  provide

TABLE III. The elastic constants ( $C_{ij}$ ) in gigapascals for the GS structures.

Material	GS	$C_{11}$	$C_{12}$	$C_{13}$	$C_{22}$	$C_{23}$	$C_{33}$	$C_{44}$	$C_{55}$	$C_{66}$
Fe <sub>2</sub> AlB <sub>2</sub> [41]	FM-O	447.0	170.1	133.9	402.7	156.4	334.6	140.2	166.3	156.2
Fe <sub>2</sub> SiB <sub>2</sub>	FM-O	427.8	202.9	154.6	433.5	179.1	326.2	51.6	136.9	83.58
Fe <sub>2</sub> GaB <sub>2</sub>	AFM-1H	387.0	118.8	86.9	387.0	87.0	337.8	134.1	84.4	84.4
Fe <sub>2</sub> InB <sub>2</sub>	AFM-1H	357.0	118.9	70.4	357.0	70.4	301.7	73.0	119.0	119.0
Mn <sub>2</sub> AlB <sub>2</sub> [41]	AFM-6O	486.0	193.5	132.1	413.1	140.0	478.4	152.2	192.2	186.9
Mn <sub>2</sub> SiB <sub>2</sub>	AFM-5O	436.4	189.0	114.7	482.1	140.5	266.2	90.4	147.5	112.8
Mn <sub>2</sub> GaB <sub>2</sub>	FM-H	370.9	121.0	84.9	370.9	84.9	334.6	106.0	106.0	125.0
Mn <sub>2</sub> InB <sub>2</sub>	AFM-3H	350.5	105.3	61.2	350.5	61.2	273.9	68.0	68.0	122.6

TABLE IV. The Young modulus ( $Y$ ), bulk modulus ( $K$ ), shear modulus ( $G$ ) in gigapascals, Pugh's ratio ( $G/K$ ), and Poisson's ratio ( $\nu$ ) for the GS structures.

Material	GS	$Y$ (GPa)	$K$ (GPa)	$G$ (GPa)	$G/K$	$\nu$
$Fe_2AlB_2$ [41]	FM-O	347.2	231.8	138.8	0.60	0.25
$Fe_2SiB_2$	FM-O	246.5	247.5	92.4	0.37	0.33
$Fe_2GaB_2$	AFM-1H	280.4	187.7	112.1	0.60	0.25
$Fe_2InB_2$	AFM-1H	250.4	169.1	99.9	0.59	0.25
$Mn_2AlB_2$ [41]	AFM-6O	407.1	256.0	164.8	0.64	0.23
$Mn_2SiB_2$	AFM-5O	296.9	219.0	116.5	0.53	0.27
$Mn_2GaB_2$	FM-H	293.7	183.5	117.5	0.64	0.23
$Mn_2InB_2$	AFM-3H	241.7	156.8	97.2	0.62	0.24

higher  $Y$ ,  $K$ , and  $G$  values than those of  $M_2GaB_2$  and  $M_2InB_2$ . We calculated the Pugh's ratio ( $G/K$ ) to investigate the brittle or ductile property of the materials. As a result of the high  $K$  of Si-based MAB phases, they exhibit a lower  $G/K$  ratio. Therefore, Al-, Ga-, and In-related  $M_2AB_2$  compounds have higher ductility relative to the Si-related counterparts. Mechanical properties are tunable in regard to the selection of the A element and the crystal structure. Comparing our calculated elastic constants with available computational literature, we noticed general agreement in terms of trends [46,47]. However, the value of the elastic constant calculated in the literature may be different than our values. This discrepancy is mainly due to missing correct spin configurations in previous work.

We should also note that there have been no experimentally determined  $C_{ij}$  values for even  $Fe_2AlB_2$  and  $Mn_2AlB_2$ . The room temperature experimental Young's moduli of  $Mn_2AlB_2$  is 243 GPa, which is  $\sim 60\%$  smaller than the predicted theoretical value [30,41]. Such a large discrepancy may not be explained solely due to the presence of 10 vol. % impurities in the experimentally measured sample and approximations implemented in the DFT calculations. In addition, the DFT calculations on some of the other MAB phases do not predict the experimentally measured elastic properties [1]. Since the synthesis of high-purity MABs is challenging, a proper comparison between experiment and theory becomes harder.

### E. Thermodynamic stability

To reveal the stability of  $M_2AB_2$  compounds, we calculated the formation energy and enthalpy. The formation energy  $\Delta E_{form}$  can be determined from the DFT computed total energy of  $M_2AB_2$  relative to the most stable bulk phases of constituent elements (i.e.,  $M$ ,  $A$ , and  $B$ ) using the following reaction;  $2M + A + 2B \rightarrow M_2AB_2$ . From this reaction, we defined  $\Delta E_{form} = E[M_2AB_2] - 2E[M] - E[A] - 2E[\alpha\text{-}B]$ . Here,  $E[M_2AB_2]$ ,  $E[M]$ ,  $E[A]$ , and  $E[\alpha\text{-}B]$  are the total energy of the optimized structure of  $M_2AB_2$ ,  $M$ ,  $A$ , and crystalline  $\alpha\text{-}B$ . Also,  $\Delta E_{form} < 0$  ensures that the target compounds are energetically stable against decomposing into the constituent elements. The calculated  $\Delta E_{form}$  values, reported in Table V, are  $\leq -0.9$  eV/unit cell, which indicates that  $M_2AB_2$  compounds are stable.

Since the calculated  $\Delta E_{form}$  values may be misleading in the interpretation of thermodynamical stability of com-

pounds, we also studied the formation enthalpy ( $\Delta H$ ) of the above MAB phases with respect to the competing phases to investigate whether these materials can be realized experimentally. Indeed, the latter is a more reliable indicator when predicting the stability. The formation enthalpy was calculated via the following expression:  $\Delta H = E[M_2AB_2] - E[\text{competing}]$ , where  $E[M_2AB_2]$  is the total energy of the MAB phase, and  $E[\text{competing}]$  is the total energy of all competing phases. We collected the stable competing phases from the Materials Project database [5]. Table V shows the most competing phases and the corresponding  $\Delta H_{comp}$  values. Negative (positive)  $\Delta H$  indicates the relative stability (instability) of MAB phases with respect to the competitive phases. In other words, the more negative (positive)  $\Delta H$  implies the higher (smaller) chance for the experimental synthesis of the predicted MAB phases. First of all, our calculations confirmed that two experimentally synthesized compounds  $Fe_2AlB_2$  and  $Mn_2AlB_2$  have negative formation enthalpies. It was reported that 80% of the inorganic compounds are expected to be stable if  $\Delta H < 0.036$  eV/atom [34,48].  $Fe_2GaB_2$  and  $Mn_2SiB_2$  exhibit  $\Delta H$  much closer to 0.036 eV/atom. More importantly,  $Mn_2GaB_2$  has  $\Delta H = 0.016$  eV/atom. When considering  $\Delta H < 0.036$  eV/atom as the phase stability criterion, we can propose that there is a possibility of synthesizing  $Fe_2GaB_2$ ,  $Mn_2GaB_2$ , and  $Mn_2SiB_2$ . In other words, they can be experimentally synthesizable even though their  $\Delta H$  values are positive. Our calculated  $\Delta H$  values and GS predictions mainly agree with work which investigated the stability of orthorhombic and hexagonal  $M_2AB_2$  phases [49].

### F. Bonding analysis

MAB phases can serve as precursors to MBene monolayers by removing the A layers. However, up to date, no completely exfoliated MBene nanosheets akin to MXenes have been successfully prepared, indicating that the chemical bonding in MAB phases must be different from that of MAX ones. MXenes are produced by selectively chemically etching the A elements from the parent MAX phase using, typically an aqueous HF solution. In the literature, selective etching processes have been employed to derive boron-based 2D MBene materials from MAB phases such as  $M_{n+1}AlB_{2n}$  and  $M_4AlB_4$  (where  $n = 1\text{--}3$ ) using HCl, HF, NaOH, and/or LiF-HCl etchants [50–52].

The etching location in MAB phases depends on the bond strength between the atoms. To evaluate the bond strengths in

TABLE V. The most competing phases and the corresponding formation enthalpies ( $\Delta H$ ) for the GS structures given in Table III. GS stands for the lowest-energy crystal and spin structure of the respective compound.

Material	GS	Most competing phases	$\Delta H$ (eV/atom)	$\Delta E_{\text{form}}$ (eV/cell)
Fe <sub>2</sub> AlB <sub>2</sub> [34]	FM-O	FeAl <sub>6</sub> , AlB <sub>2</sub> , FeB	-0.078	
Fe <sub>2</sub> SiB <sub>2</sub>	FM-O	Fe <sub>2</sub> B <sub>7</sub> , FeSi, FeB	0.107	-1.268
Fe <sub>2</sub> GaB <sub>2</sub>	AFM-1H	Fe <sub>2</sub> B <sub>7</sub> , FeB, FeGa <sub>3</sub>	0.037	-1.467
Fe <sub>2</sub> InB <sub>2</sub>	AFM-1H	FeB, In	0.129	-0.900
Mn <sub>2</sub> AlB <sub>2</sub> [34]	AFM-6O	Mn <sub>4</sub> Al <sub>11</sub> , MnB, MnB <sub>4</sub>	-0.060	
Mn <sub>2</sub> SiB <sub>2</sub>	AFM-5O	Mn <sub>4</sub> Si <sub>7</sub> , Mn <sub>3</sub> B <sub>4</sub> , MnB <sub>4</sub>	0.039	-1.833
Mn <sub>2</sub> GaB <sub>2</sub>	FM-H	MnGa <sub>4</sub> , Mn <sub>3</sub> B <sub>4</sub> , Mn <sub>2</sub> B	0.016	-1.684
Mn <sub>2</sub> InB <sub>2</sub>	AFM-3H	Mn <sub>3</sub> B <sub>4</sub> , Mn <sub>2</sub> B, In	0.104	-1.105

the considered MAB phases, we employed the crystal orbital Hamilton population (COHP) analysis [34]. In the COHP analysis, we split the band-structure energy into bonding, nonbonding, and antibonding contributions using localized atomic basis sets. The energy integration of all COHPs for a pair of atoms up to the Fermi energy (ICOHP) can be used to qualify bond strength [53]. The Local Orbital Basis Suite Towards Electronic-Structure Reconstruction code is utilized for the COHP calculations with the pbeVaspFit2015 basis set [54–56].

It should be noted that the ICOHP mainly measures the strength of the covalency of a bond. A lower ICOHP value corresponds to a stronger covalent bond. Table VI summarizes ICOHP values for Fe<sub>2</sub>GaB<sub>2</sub>, Mn<sub>2</sub>GaB<sub>2</sub>, and Mn<sub>2</sub>SiB<sub>2</sub> because these compounds have much higher synthesization chances than other compounds. To elucidate the impact of crystal structure on the nature of covalent bonding, we included all three crystal symmetries for the considered MAB phases. As the strength of a chemical bond depends on the distance between the atoms, the ICOHP values vary as a function of atom-atom separation. For instance, while the ICOHP value is  $<-5.81$  eV for the B-B bond in the hexagonal and orthorhombic phases, it reduces to values  $\sim-0.30$  eV in the tetragonal phase where the B-B interatomic distance is much larger than the hexagonal and orthorhombic phases (1.7 vs 2.5 Å). Our COHP analyses find that Fe-Fe and Mn-Mn bonds display a weak covalent nature regardless of the crystal symmetry and

spin configuration. Fe-B or Mn-B bonding exhibits a fair crystal structure dependency. The strength of covalent bonding between transition metal and B atom enhances H  $\rightarrow$  O  $\rightarrow$  T owing to the fact that the M-B bond length decreases as T  $\rightarrow$  O  $\rightarrow$  H. In the orthorhombic structures with Ga as the A element, the transition metal-Ga bond is very weak with ICOHP values  $\sim-0.01$  eV. It may be inferred that the etching out of Ga from the corresponding MAB phases may lead to the formation of MBenes. However, when one considers the B-Ga bonding, which is strong (such as for the Fe case) as a result of direct bond formation, it can be unlikely to isolate intact MBene layers by etching out the Ga layer from the parent compound.

However, in the hexagonal phase, the transition metal layer separates the B layer from the A layer, thereby leading to a weak covalent interaction. Considering the lowest-energy crystal structures and spin configurations for each transition metal-A element combination (i.e., Fe<sub>2</sub>GaB<sub>2</sub>-AFM-1H, Mn<sub>2</sub>GaB<sub>2</sub>-FM-H, and Mn<sub>2</sub>SiB<sub>2</sub>-AFM-5O), our ICOHP analysis found that the possible etching position within corresponding MAB phases depends on the compound. For instance, in H-Fe<sub>2</sub>GaB<sub>2</sub>, the Fe-Ga bond is stronger than Fe-B, meaning that this compound prefers to be separated between the Fe and B layers. However, O-Mn<sub>2</sub>SiB<sub>2</sub> with AFM-5O prefers to be etched out from the Mn-Si bond. However, the M-A bonds are stronger than the M-B ones in H-Fe<sub>2</sub>GaB<sub>2</sub> and H-Mn<sub>2</sub>GaB<sub>2</sub>, suggesting that it may be

TABLE VI. Integrated COHP (in electronvolts) up to the Fermi level for different bonds in  $M_2AB_2$ , where  $M = \text{Fe}$  and  $\text{Mn}$ , and  $A = \text{Ga}$  and  $\text{Si}$ . Here, SC stands for the lowest-energy spin configuration of the respective compound. We only considered the compounds with  $\Delta H < 40$  meV/atom (i.e., Fe<sub>2</sub>GaB<sub>2</sub>-AFM-1H, Mn<sub>2</sub>GaB<sub>2</sub>-FM-H, and Mn<sub>2</sub>SiB<sub>2</sub>-AFM-5O). We also included the other crystal structures of these compounds to understand dependency of bonding on the crystal structure.

MAB Phase	SC	$M\text{-}M$	$M\text{-}B$	$M\text{-}A$	$B\text{-}A$	$B\text{-}B$	$A\text{-}A$
H-Fe <sub>2</sub> GaB <sub>2</sub>	AFM-1H	-0.19	-1.28	-1.43	-0.32	-6.61	-1.44
O-Fe <sub>2</sub> GaB <sub>2</sub>	FM-O	-0.10	-1.40	-0.01	-3.32	-6.39	-1.84
T-Fe <sub>2</sub> GaB <sub>2</sub>	AFM-3T	-0.20	-2.40	-0.99	-3.10	-0.39	-1.46
H-Mn <sub>2</sub> SiB <sub>2</sub>	AFM-3H	-0.28	-1.36	-1.89	-0.30	-6.26	-0.95
O-Mn <sub>2</sub> SiB <sub>2</sub>	AFM-5O	-0.20	-1.50	-1.30	-4.23	-5.81	-1.44
T-Mn <sub>2</sub> SiB <sub>2</sub>	AFM-3T	-0.30	-2.37	-1.30	-3.97	-0.41	-0.85
H-Mn <sub>2</sub> GaB <sub>2</sub>	FM-H	-0.28	-1.43	-1.49	-0.26	-6.48	-1.38
O-Mn <sub>2</sub> GaB <sub>2</sub>	AFM-5O	-0.20	-1.65	-0.01	-0.01	-6.35	-1.80
T-Mn <sub>2</sub> GaB <sub>2</sub>	AFM-3T	-0.25	-2.57	-1.10	-2.40	-0.36	-1.49

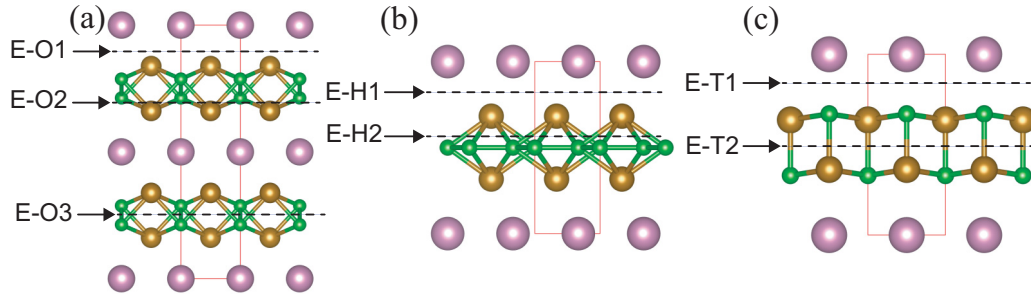


FIG. 6. The possible location for the separation of MAB crystals with (a) orthorhombic, (b) hexagonal, and (c) tetragonal. Green, purple, and dark yellow spheres represent the B, A, and  $M$  atoms, respectively.

hard to isolate the  $M$ -B layer from the corresponding MAB phases via etching the A layer without affecting the integrity of the MBene. Similarly, the  $M$ -B bond is stronger than the  $M$ -A bond, but the B-A bond is stronger than both in O- and T- $\text{Mn}_2\text{SiB}_2$ , which makes it complicated to isolate an intact MBene layer.

#### G. Work of separation

To shed more light on the etching process in the MAB phases, we also calculated the work of separation. In this process, we separated the MAB crystals from different identified positions which are denoted in Fig. 6. We separated the orthorhombic crystal (1) between the transition metal and A layers [called E-O1 in Fig. 6(a)], (2) between two boron layers within the  $M$ -B slab (E-O2), and (3) between the transition metal and B layers (E-O3). Similarly, E-H1

(E-H2) in Fig. 6(b) represents the separation of the crystal between the transition metal and A layers (transition metal and B layers) for the hexagonal crystal structure. For the tetragonal phase, we identified two positions, namely, E-T1 (between transition metal-B and A layers) and E-T2 (between two transition metal-B layers within the  $M$ -B slab). For H- $\text{Fe}_2\text{GaB}_2$  in the AFM-1 configuration, our calculations found that the separation from E-H1 (i.e., breaking of the Fe-Ga bond) is energetically more favorable than E-H2 by 0.208 eV/ $\text{\AA}^2$ , which contradicts the COHP calculations where we predicted that the Fe-Ga bond is stronger than the Fe-B bond. This discrepancy can be explained by counting the number of bonds broken in E-H1 and E-H2, which is three (six) in the former (latter) case. We obtained similar behavior for FM hexagonal  $\text{Mn}_2\text{GaB}_2$ , where the separation from E-H1 is more favorable than E-H2 by 0.160 eV/ $\text{\AA}^2$ . Finally, for orthorhombic  $\text{Mn}_2\text{SiB}_2$ , our ICOHP and work of separation calculations

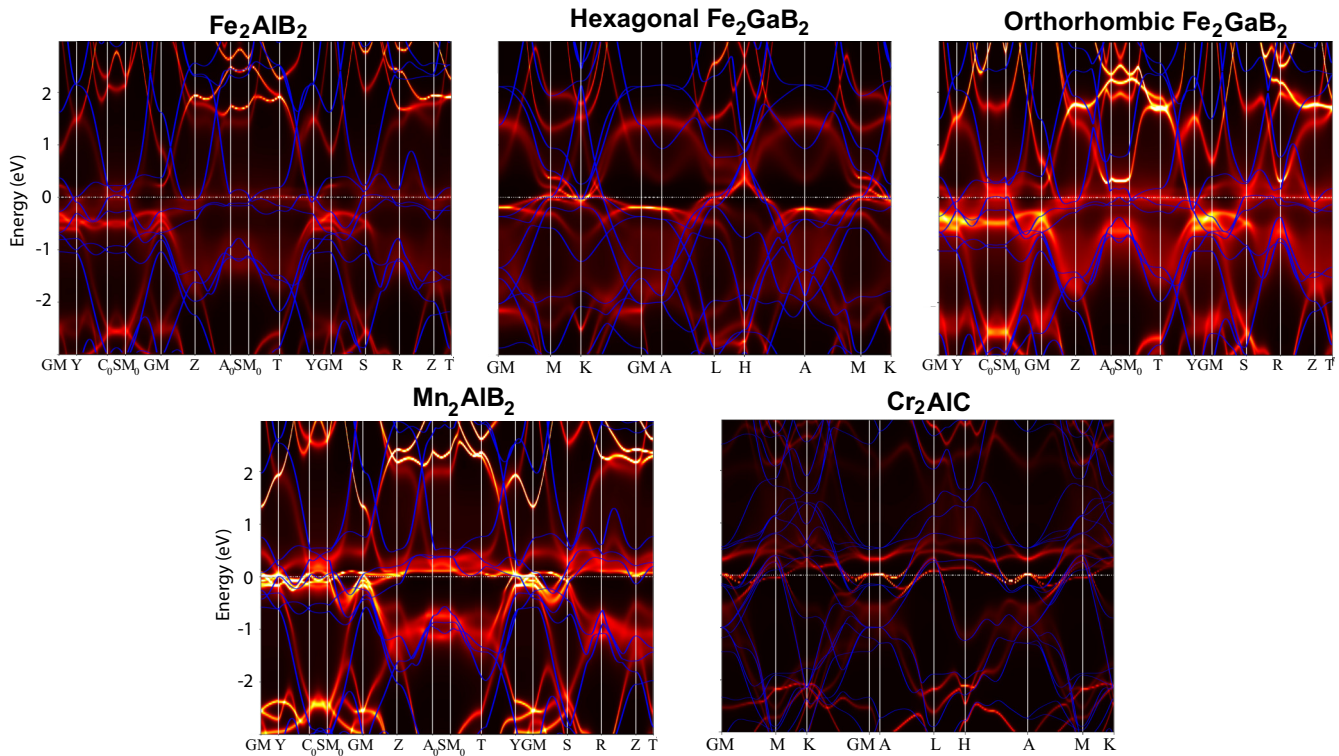


FIG. 7. The spectral functions of borides  $\text{Fe}_2\text{AlB}_2$ ,  $\text{Fe}_2\text{GaB}_2$ , and  $\text{Mn}_2\text{AlB}_2$ , as well as the MAX compound  $\text{Cr}_2\text{AlC}$  for comparison, from DFT+eDMFT. The DFT+LDA band structure is also shown as blue lines.

predicted consistent results, where the Mn-Si bond is weaker than the Mn-B and B-B bonds. However, due to stronger B-Si interaction, the separation of this compound from E-O1 seems to be challenging. Our results indicate that the B-A bond strength is one of the main factors for challenging exfoliation of MAB compounds into MBenes.

## H. DMFT calculations

To assess the strength of correlations in the paramagnetic phase of the MAB materials, we performed DFT+eDMFT calculations. The Kohn-Sham DFT-based approaches can reproduce magnetically ordered phases as well as phases where atomic magnetic moments do not exist. Unlike these approaches, DFT+eDMFT can reproduce paramagnetic phases of transition metal-based compounds, where the local magnetic moments exist but are fluctuating [25].

In Fig. 7, we show the spectral functions of borides  $\text{Fe}_2\text{AlB}_2$ ,  $\text{Fe}_2\text{GaB}_2$ , and  $\text{Mn}_2\text{AlB}_2$  as well as the MAX compound  $\text{Cr}_2\text{AlC}$  for comparison. ARPES measurements on  $\text{Cr}_2\text{AlC}$  show that this material has nonnegligible correlation-induced mass enhancement, which leads to an overestimation of the bandwidth by DFT [57]. Our DFT+eDMFT results confirm this observation and show that the electronic structures of all the MAB compounds we considered deviate from the DFT predictions by comparable amounts to  $\text{Cr}_2\text{AlC}$ . However, the bandwidth renormalization with respect to DFT  $Z = m_{\text{DFT}}^*/m_{\text{DMFT}}^*$  as calculated from the linear part of the electronic self-energy is only in the range of  $Z \sim 0.65\text{--}0.75$  in all compounds, which indicates that these materials are not very strongly correlated Fermi liquids. The strength of the mass renormalization we observe is roughly in line with the values reported for  $\text{Fe}_2\text{AlB}_2$  in Ref. [58] from the comparison of experimental data with DFT results. However, we do not predict a strong deviation from the Fermi-liquid behavior. We also note the relatively diffuse nature of the bands and the nonzero values of the imaginary parts of the self-energies near zero (not shown), as observed in another DMFT study on the MAX compound  $\text{Mn}_2\text{GaC}$  as well [59].

In the hexagonal  $M_2\text{AB}_2$  structure with space group  $P\bar{6}m2$ , the transition metal is on the  $2h$  Wyckoff position with site symmetry of  $3m$ . This splits the  $d$  orbitals into  $2 + 2 + 1$ , where the  $(xz, yz)$  doublet is  $\sim 2$  eV lower in energy than the other  $d$  orbitals. In the orthorhombic phase with space group  $Cmmm$ , the site symmetry of the transition metal ion is reduced to  $2mm$  (Wyckoff position  $4j$ ), which splits all 5  $d$  orbitals. Nevertheless, the most significant energy splitting is still between  $xz$  and  $yz$  orbitals (which are no longer degenerate) and the other 3  $d$  orbitals. There is no significant orbital selectivity in the self-energy near zero, and the slope of the self-energy for all orbitals is comparable at the temperature we considered ( $T \sim 213$  K).

In all the compounds we studied using DFT+eDMFT, the expectation value of the square of the spin  $\langle S_z^2 \rangle$  in the paramagnetic phase is in the range 0.9–1.2, despite the different numbers of  $d$  electrons in each compound. As a result, all the studied compounds are in the intermediate spin range. Note that this is the magnitude of the fluctuating magnetic moments in the paramagnetic phase and is expected to be smaller than the ordered moment in the magnetically ordered

phases predicted by DFT. Our results are in line with the DMFT predictions on the paramagnetic phase of the AFM compound  $\text{Mn}_2\text{GaC}$ , which has a spin moment of  $\langle S_z^2 \rangle = 1.7$  on the Mn site [59]. While the local moment in the MAB compounds is usually smaller than that in  $\text{Mn}_2\text{GaC}$  by DMFT [59], it is nevertheless nonnegligable. This suggests that these compounds form fluctuating local magnetic moments above the magnetic transition temperatures, and even if they were not magnetically ordered, they would be reasonably close to a magnetic quantum critical point and be driven into magnetic ordering by doping, as is the case in  $\text{Cr}_2\text{GeC}$  [6].

## IV. CONCLUSIONS

In summary, we investigated three different crystal structures, namely, orthorhombic, hexagonal, and tetragonal, for  $\text{Fe}_2\text{AB}_2$  and  $\text{Mn}_2\text{AB}_2$  MAB phases with  $A = \text{Ga}, \text{In}$ , and  $\text{Si}$ . To properly treat  $d$  electrons of Fe and Mn atoms, we considered three different methods, namely, PBE-GGA, PBE-GGA+ $U$ , and SCAN. Our calculations depicted that the structural and magnetic properties of experimentally sensitized  $\text{Fe}_2\text{AlB}_2$  and  $\text{Mn}_2\text{AlB}_2$  are well described by PBE-GGA, meaning that semilocal functionals are appropriate for MAB phases. Depending on the  $M$  and  $A$  elements, we can realize different crystal structures with various magnetic states. The phonons and elastic coefficient calculations suggest that the considered MAB phases are dynamically and mechanically stable. We found that orthorhombic and hexagonal

TABLE VII. Magnetic GS predicted using PBE+ $U$  (where  $U = 0, 2$ , and 3 eV) and SCAN.

Material	$U = 0$	$U = 2$	$U = 3$	SCAN
$\text{Fe}_2\text{AlB}_2\text{-O}$	FM	FM	FM	FM
$\text{Fe}_2\text{AlB}_2\text{-H}$	AFM-1	AFM-1	AFM-1	AFM-1
$\text{Fe}_2\text{AlB}_2\text{-T}$	AFM-3	AFM-3	FM	AFM-3
$\text{Fe}_2\text{SiB}_2\text{-O}$	FM	FM	FM	FM
$\text{Fe}_2\text{SiB}_2\text{-H}$	AFM-1	AFM-1	AFM-1	AFM-1
$\text{Fe}_2\text{SiB}_2\text{-T}$	AFM-3	FM	FM	FM
$\text{Fe}_2\text{GaB}_2\text{-O}$	FM	FM	AFM-6	FM
$\text{Fe}_2\text{GaB}_2\text{-H}$	AFM-1	AFM-1	AFM-1	AFM-1
$\text{Fe}_2\text{GaB}_2\text{-T}$	AFM-3	AFM-3	AFM-3	AFM-3
$\text{Fe}_2\text{InB}_2\text{-O}$	AFM-3	AFM-5	AFM-5	AFM-5
$\text{Fe}_2\text{InB}_2\text{-H}$	AFM-1	AFM-1	AFM-1	AFM-1
$\text{Fe}_2\text{InB}_2\text{-T}$	AFM-3	AFM-3	AFM-3	AFM-3
$\text{Mn}_2\text{AlB}_2\text{-O}$	AFM-6	AFM-6	AFM-6	AFM-6
$\text{Mn}_2\text{AlB}_2\text{-H}$	FM	AFM-1	AFM-1	AFM-1
$\text{Mn}_2\text{AlB}_2\text{-T}$	AFM-3	AFM-3	AFM-3	AFM-3
$\text{Mn}_2\text{SiB}_2\text{-O}$	AFM-6	AFM-6	FM	AFM-6
$\text{Mn}_2\text{SiB}_2\text{-H}$	AFM-3	AFM-1	AFM-1	AFM-1
$\text{Mn}_2\text{SiB}_2\text{-T}$	AFM-3	AFM-3	AFM-3	AFM-3
$\text{Mn}_2\text{GaB}_2\text{-O}$	AFM-6	AFM-6	AFM-6	AFM-6
$\text{Mn}_2\text{GaB}_2\text{-H}$	FM	AFM-1	AFM-1	AFM-1
$\text{Mn}_2\text{GaB}_2\text{-O}$	AFM-3	AFM-3	AFM-3	AFM-3
$\text{Mn}_2\text{InB}_2\text{-O}$	NM	AFM-5	AFM-6	AFM-5
$\text{Mn}_2\text{InB}_2\text{-H}$	AFM-3	AFM-1	AFM-1	AFM-1
$\text{Mn}_2\text{InB}_2\text{-T}$	FM	AFM-3	AFM-3	AFM-3

MAB phases are energetically favorable over the tetragonal one for all  $M$  and  $A$  elements. The formation enthalpy computed relative to competing phases shows that hexagonal  $\text{Mn}_2\text{GaB}_2$  has a higher chance of experimental realization, followed by hexagonal  $\text{Fe}_2\text{GaB}_2$  and orthorhombic  $\text{Mn}_2\text{SiB}_2$ . We characterized the bond strength between various atoms by computing ICOHP. Moreover, the work of separation was computed. The calculated work of separation values indicate that the MAB phases which have a high chance of experimental realization are preferably separated between the transition metal and  $A$  element layers, which makes it possible to form MBenes from the parent compounds. However, the computed ICOHP values suggest that it may be hard to isolate intact MBene layers by etching  $A$  layers from the MAB phases. Generally, the B-A bond strength obstructs the exfoliation process. DFT+eDMFT calculations suggest that these materials are not strongly correlated; nevertheless, all of them seem to have significant magnetic moments in the paramagnetic phase. While these moments are smaller than those in the magnetically ordered phases, so the exchange field is important in

stabilizing larger spins, they indicate that even the materials that do not spontaneously order would likely be driven into a magnetic phase by doping.

## ACKNOWLEDGMENTS

This paper is supported by the Air Force Office of Scientific Research under Award No. FA9550-21-1-0208. O.E. acknowledges support from National Science Foundation Award No. DMR 1904716.

## APPENDIX

In Table VII, we notice that the magnetic GS depends to some extent on the functional. Increasing the  $U$  parameter favors the AFM exchange interaction either within or between the nearest Fe/Mn-B layers. Regardless of functional, the hexagonal and tetragonal Fe-based MAB phases mainly prefer the AFM configuration as the lowest-energy magnetic order.

- 
- [1] S. Kota, M. Sokol, and M. W. Barsoum, A progress report on the MAB phases: atomically laminated, ternary transition metal borides, *Int. Mater. Rev.* **65**, 226 (2020).
  - [2] J. Wang, T.-N. Ye, Y. Gong, J. Wu, N. Miao, T. Tada, and H. Hosono, Discovery of hexagonal ternary phase  $\text{Ti}_2\text{InB}_2$  and its evolution to layered boride  $\text{TiB}$ , *Nat. Commun.* **10**, 2284 (2019).
  - [3] R. Wang, X. Tao, Y. Ouyang, H. Chen, and Q. Peng, Suggest a new approach to fabricate  $\text{AlFe}_2\text{B}_2$ , *Comput. Mater. Sci.* **171**, 109239 (2020).
  - [4] D. Potashnikov, E. Caspi, A. Pesach, A. Hoser, S. Kota, L. Verger, M. Barsoum, I. Felner, A. Keren, and O. Rivin, Magnetic ordering in the nano-laminar ternary  $\text{Mn}_2\text{AlB}_2$  using neutron and x-ray diffraction, *J. Magn. Magn. Mater.* **471**, 468 (2019).
  - [5] A. Jain, S. P. Ong, G. Hautier, W. Chen, W. D. Richards, S. Dacek, S. Cholia, D. Gunter, D. Skinner, G. Ceder *et al.*, The Materials Project: a materials genome approach to accelerating materials innovation, *APL Mater.* **1**, 011002 (2013).
  - [6] Z. Liu, T. Waki, Y. Tabata, and H. Nakamura, Mn-doping-induced itinerant-electron ferromagnetism in  $\text{Cr}_2\text{GeC}$ , *Phys. Rev. B* **89**, 054435 (2014).
  - [7] G. Kresse and J. Hafner, *Ab initio* molecular dynamics for liquid metals, *Phys. Rev. B* **47**, 558(R) (1993).
  - [8] G. Kresse and J. Hafner, *Ab initio* molecular-dynamics simulation of the liquid-metal–amorphous–semiconductor transition in germanium, *Phys. Rev. B* **49**, 14251 (1994).
  - [9] J. F. G. Kresse, Efficiency of *ab initio* total energy calculations for metals and semiconductors using a plane-wave basis set, *Comput. Mater. Sci.* **6**, 15 (1996).
  - [10] G. Kresse and J. Furthmüller, Efficient iterative schemes for *ab initio* total-energy calculations using a plane-wave basis set, *Phys. Rev. B* **54**, 11169 (1996).
  - [11] P. E. Blöchl, Projector augmented-wave method, *Phys. Rev. B* **50**, 17953 (1994).
  - [12] G. Kresse and D. Joubert, From ultrasoft pseudopotentials to the projector augmented-wave method, *Phys. Rev. B* **59**, 1758 (1999).
  - [13] J. P. Perdew, K. Burke, and M. Ernzerhof, Generalized Gradient Approximation Made Simple, *Phys. Rev. Lett.* **77**, 3865 (1996); **78**, 1396(E) (1997).
  - [14] R. Elmér, M. Berg, L. Carlén, B. Jakobsson, B. Norén, A. Oskarsson, G. Ericsson, J. Julien, T. F. Thorsteinsen, M. Guttormsen *et al.*,  $K^+$  Emission in Symmetric Heavy Ion Reactions at Subthreshold Energies, *Phys. Rev. Lett.* **77**, 4884 (1996).
  - [15] J. Sun, A. Ruzsinszky, and J. P. Perdew, Strongly Constrained and Appropriately Normed Semilocal Density Functional, *Phys. Rev. Lett.* **115**, 036402 (2015).
  - [16] S. L. Dudarev, G. A. Botton, S. Y. Savrasov, C. J. Humphreys, and A. P. Sutton, Electron-energy-loss spectra and the structural stability of nickel oxide: an LSDA + $U$  study, *Phys. Rev. B* **57**, 1505 (1998).
  - [17] D. A. Kitchev, H. Peng, Y. Liu, J. Sun, J. P. Perdew, and G. Ceder, Energetics of  $\text{MnO}_2$  polymorphs in density functional theory, *Phys. Rev. B* **93**, 045132 (2016).
  - [18] C. Shahi, J. Sun, and J. P. Perdew, Accurate critical pressures for structural phase transitions of group IV, III-V, and II-VI compounds from the SCAN density functional, *Phys. Rev. B* **97**, 094111 (2018).
  - [19] Y. Hinuma, H. Hayashi, Y. Kumagai, I. Tanaka, and F. Oba, Comparison of approximations in density functional theory calculations: energetics and structure of binary oxides, *Phys. Rev. B* **96**, 094102 (2017).
  - [20] Y. Zhang, J. Sun, J. P. Perdew, and X. Wu, Comparative first-principles studies of prototypical ferroelectric materials by LDA, GGA, and SCAN meta-GGA, *Phys. Rev. B* **96**, 035143 (2017).
  - [21] A. Togo and I. Tanaka, First principles phonon calculations in materials science, *Scr. Mater.* **108**, 1 (2015).
  - [22] S. Baroni, S. de Gironcoli, A. Dal Corso, and P. Giannozzi, Phonons and related crystal properties from density-functional perturbation theory, *Rev. Mod. Phys.* **73**, 515 (2001).
  - [23] K. Haule, Quantum Monte Carlo impurity solver for cluster dynamical mean-field theory and electronic structure calculations with adjustable cluster base, *Phys. Rev. B* **75**, 155113 (2007).

- [24] K. Haule, C.-H. Yee, and K. Kim, Dynamical mean-field theory within the full-potential methods: Electronic structure of CeIrIn<sub>5</sub>, CeCoIn<sub>5</sub>, and CeRhIn<sub>5</sub>, *Phys. Rev. B* **81**, 195107 (2010).
- [25] A. Paul and T. Birol, Applications of DFT+DMFT in Materials Science, *Annu. Rev. Mater. Res.* **49**, 31 (2019).
- [26] K. Haule, T. Birol, and G. Kotliar, Covalency in transition-metal oxides within all-electron dynamical mean-field theory, *Phys. Rev. B* **90**, 075136 (2014).
- [27] Q. Han, H. T. Dang, and A. J. Millis, Ferromagnetism and correlation strength in cubic barium ruthenate in comparison to strontium and calcium ruthenate: a dynamical mean-field study, *Phys. Rev. B* **93**, 155103 (2016).
- [28] A. Paul and T. Birol, Strain tuning of plasma frequency in vanadate, niobate, and molybdate perovskite oxides, *Phys. Rev. Mater.* **3**, 085001 (2019).
- [29] J. Liu, S. Li, B. Yao, S. Hu, J. Zhang, W. Yu, and Y. Zhou, Rapid synthesis and characterization of a nanolaminated Fe<sub>2</sub>AlB<sub>2</sub> compound, *J. Alloys Compd.* **766**, 488 (2018).
- [30] S. Kota, Y. Chen, J. Wang, S. J. May, M. Radovic, and M. W. Barsoum, Synthesis and characterization of the atomic laminate Mn<sub>2</sub>AlB<sub>2</sub>, *J. Eur. Ceram. Soc.* **38**, 5333 (2018).
- [31] X. Tan, P. Chai, C. M. Thompson, and M. Shatruk, Magnetocaloric effect in AlFe<sub>2</sub>B<sub>2</sub>: toward magnetic refrigerants from earth-abundant elements, *J. Am. Chem. Soc.* **135**, 9553 (2013), pMID: 23731263.
- [32] S. P. Bennett, S. Kota, H. ElBidweihy, J. F. Parker, L. A. Hanner, P. Finkel, and M. W. Barsoum, Magnetic and magnetocaloric properties of Fe<sub>2</sub>AlB<sub>2</sub> synthesized by single-step reactive hot pressing, *Scr. Mater.* **188**, 244 (2020).
- [33] M. Ade and H. Hillebrecht, Ternary borides Cr<sub>2</sub>AlB<sub>2</sub>, Cr<sub>3</sub>AlB<sub>4</sub>, and Cr<sub>4</sub>AlB<sub>6</sub>: the first members of the series (CrB<sub>2</sub>)<sub>n</sub>CrAl with  $n = 1, 2, 3$  and a unifying concept for ternary borides as MAB-phases, *Inorg. Chem.* **54**, 6122 (2015).
- [34] M. Khazaei, J. Wang, M. Estili, A. Ranjbar, S. Suehara, M. Arai, K. Esfarjani, and S. Yunoki, Novel MAB phases and insights into their exfoliation into 2D MBenes, *Nanoscale* **11**, 11305 (2019).
- [35] I. Ozdemir, Y. Kadioglu, Y. Yüksel, Ü. Akinci, O. Ü. Aktürk, E. Aktürk, and S. Ciraci, Columnar antiferromagnetic order of a mbene monolayer, *Phys. Rev. B* **103**, 144424 (2021).
- [36] D. Hedlund, J. Cedervall, A. Edström, M. Werwiński, S. Kontos, O. Eriksson, J. Rusz, P. Svedlindh, M. Sahlberg, and K. Gunnarsson, Magnetic properties of the Fe<sub>5</sub>SiB<sub>2</sub>-Fe<sub>5</sub>Pb<sub>2</sub> system, *Phys. Rev. B* **96**, 094433 (2017).
- [37] M. Dahlqvist, J. Zhou, I. Persson, B. Ahmed, J. Lu, J. Halim, Q. Tao, J. Palisaitis, J. Thörnberg, P. Helmer *et al.*, Out-of-plane ordered laminate borides and their 2D Ti-based derivative from chemical exfoliation, *Adv. Mater.* **33**, 2008361 (2021).
- [38] M. Dahlqvist and J. Rosen, Chemical order or disorder—a theoretical stability expose for expanding the compositional space of quaternary metal borides, *Mater. Adv.* **3**, 2908 (2022).
- [39] M. Ekholm, D. Gambino, H. J. M. Jönsson, F. Tasnádi, B. Alling, and I. A. Abrikosov, Assessing the SCAN functional for itinerant electron ferromagnets, *Phys. Rev. B* **98**, 094413 (2018).
- [40] M. Born and K. Huang, *Dynamical Theory of Crystal Lattices* (Clarendon Press, Oxford, 1954).
- [41] K. Kádas, D. Iuşan, J. Hellsvik, J. Cedervall, P. Berastegui, M. Sahlberg, U. Jansson, and O. Eriksson, AlM<sub>2</sub>B<sub>2</sub>(M = Cr, Mn, Fe, Co, Ni): a group of nanolaminated materials, *J. Phys.: Condens. Matter* **29**, 155402 (2017).
- [42] W. Voigt, *Lehrbuch der Kristallphysik* (Teubner, Leipzig, 1928), Vol. 962.
- [43] A. Reuss, Berechnung der Fließgrenze von Mischkristallen auf Grund der Plastizitätsbedingung für Einkristalle, *Z. angew. Math. Mech.* **9**, 49 (1929).
- [44] R. Hill, The elastic behaviour of a crystalline aggregate, *Proc. Phys. Soc. A* **65**, 349 (1952).
- [45] E. M. D. Siriwardane, R. P. Joshi, N. Kumar, and D. Çkir, Revealing the formation energy-exfoliation energy-structure correlation of MAB phases using machine learning and DFT, *ACS Appl. Mater. Interfaces* **12**, 29424 (2020).
- [46] X. Liu, X. Ge, R. Si, M. Zhang, and X. Xu, A survey investigation on the stability, electronic and elastic properties of hexagonal ternary transition-metal borides by first-principles calculations, *Vacuum* **177**, 109432 (2020).
- [47] Y. Liu, Z. Jiang, X. Jiang, and J. Zhao, New refractory MAB phases and their 2D derivatives: insight into the effects of valence electron concentration and chemical composition, *RSC Adv.* **10**, 25836 (2020).
- [48] Y. Wu, P. Lazic, G. Hautier, K. Persson, and G. Ceder, First principles high throughput screening of oxynitrides for water-splitting photocatalysts, *Energy Environ. Sci.* **6**, 157 (2013).
- [49] A. Carlsson, J. Rosen, and M. Dahlqvist, Theoretical predictions of phase stability for orthorhombic and hexagonal ternary MAB phases, *Phys. Chem. Chem. Phys.* **24**, 11249 (2022).
- [50] L. T. Alameda, C. F. Holder, J. L. Fenton, and R. E. Schaak, Partial etching of Al from MoAlB single crystals to expose catalytically active basal planes for the hydrogen evolution reaction, *Chem. Mater.* **29**, 8953 (2017).
- [51] L. T. Alameda, R. W. Lord, J. A. Barr, P. Moradifar, Z. P. Metzger, B. C. Steimle, C. F. Holder, N. Alem, S. B. Sinnott, and R. E. Schaak, Multi-step topochemical pathway to metastable Mo<sub>2</sub>AlB<sub>2</sub> and related two-dimensional nanosheet heterostructures, *J. Am. Chem. Soc.* **141**, 10852 (2019).
- [52] K. Kim, C. Chen, D. Nishio-Hamane, M. Okubo, and A. Yamada, Topochemical synthesis of phase-pure Mo<sub>2</sub>AlB<sub>2</sub> through staging mechanism, *Chem. Commun.* **55**, 9295 (2019).
- [53] M. Küpers, P. M. Konze, S. Maintz, S. Steinberg, A. M. Mio, O. Cojocaru-Mirédin, M. Zhu, M. Müller, M. Luysberg, J. Mayer *et al.*, Unexpected Ge-Ge contacts in the two-dimensional Ge<sub>4</sub>Se<sub>3</sub>Te phase and analysis of their chemical cause with the density of energy (DOE) function, *Angew. Chem. Int. Ed.* **56**, 10204 (2017).
- [54] V. L. Deringer, A. L. Tchougréeff, and R. Dronskowski, Crystal orbital hamilton population (COHP) analysis as projected from plane-wave basis sets, *J. Phys. Chem. A* **115**, 5461 (2011).
- [55] S. Maintz, V. L. Deringer, A. L. Tchougréeff, and R. Dronskowski, Analytic projection from plane-wave and PAW

- wavefunctions and application to chemical-bonding analysis in solids, *J. Comput. Chem.* **34**, 2557 (2013).
- [56] S. Maintz, V. L. Deringer, A. L. Tchougréeff, and R. Dronskowski, LOBSTER: a tool to extract chemical bonding from plane-wave based DFT, *J. Comput. Chem.* **37**, 1030 (2016).
- [57] T. Ito, D. Pinek, T. Fujita, M. Nakatake, S.-I. Ideta, K. Tanaka, and T. Ouisse, Electronic structure of Cr<sub>2</sub>AlC as observed by angle-resolved photoemission spectroscopy, *Phys. Rev. B* **96**, 195168 (2017).
- [58] Z. Liu, S. Yang, H. Su, L. Zhou, X. Lu, Z. Liu, J. Gao, Y. Huang, D. Shen, Y. Guo *et al.*, Non-Fermi-liquid behavior and saddlelike flat band in the layered ferromagnet AlFe<sub>2</sub>B<sub>2</sub>, *Phys. Rev. B* **101**, 245129 (2020).
- [59] H. J. M. Jönsson, M. Ekholm, I. Leonov, M. Dahlqvist, J. Rosen, and I. A. Abrikosov, Correlation strength, orbital-selective incoherence, and local moments formation in the magnetic MAX-phase Mn<sub>2</sub>GaC, *Phys. Rev. B* **105**, 035125 (2022).